Eur. J. Mech. B - Fluids 20 (2001) 821–840

S0997-7546(01)01155-4/FLA

Low-dimensional model for vortex merging in the two-dimensional temporal mixing layer

W.L. IJzerman [a,*], E. van Groesen [b]

[a] *Philips Research, Prof. Holstlaan 4, 5656 AA Eindhoven, The Netherlands*
[b] *University of Twente, Faculty of Mathematical Sciences, P.O. Box 217, 7500AE Enschede, The Netherlands*

(Received 28 June 2000; revised 25 April 2001; accepted 5 July 2001)

Abstract – The two-dimensional temporal mixing layer shows spiraling and merging vortices and is an example of a flow problem in which, despite the complexity, the vortices as individual coherent structures can be clearly visualized. In this paper we present a method for the analysis of the data that describes the spiraling and merging of vortices. To that end we define a parameterized set of structures, the 'phenomenological model manifold', which approximates the apparent spatial structures. Then we let the parameters of the manifold vary in such a way that the succession of states resembles the evolving flow as well as possible. Two different model manifolds were designed, one model for which the vortices are described with Gaussian profiles, and another in which a more optimal spatial structure is used. Projection of the numerical data on these manifolds results in information about the strength, ellipticity and trajectories of the vortices. The method is also used to study the successive merging of vortices; differing from scaling arguments for an inviscid flow, the results show that the first pairwise merging evolves approximately 2.11 times faster than the second merging. Efficient procedures are described for the required extensive optimisation problems. © 2001 Éditions scientifiques et médicales Elsevier SAS

mixing layer / signal representation / signal analysis / low-dimensional models

1. Introduction

In this paper we model the spiraling behavior and the merging of vortices in the temporal mixing layer. The temporal mixing layer is a simplification of the (real) spatial mixing layer found behind a splitter plate. For specific initial conditions instabilities will grow and vortices will appear. Pairs of vortices start to spiral around each other and merge into a new vortex. The spiraling behavior and the pairwise merging will repeat itself with the newly formed vortices till only one vortex is left in the considered domain.

The dynamic model to be constructed consist of a succession in time in a so-called phenomenological model manifold $\mathcal{PM}$. This $\mathcal{PM}$ is a set of spatial structures that resemble various spatial manifestations that may occur in the real dynamics. Different elements in the set are characterised by different values of parameters; the numerical data are used to determine the evolution of the parameters.

Symbolically, if p denote the parameters, one spatial configuration in the phenomenological model manifold can be represented as $\zeta(p)(x)$. Then an evolution is obtained by allowing p to depend on time, $p(t)$. If $S(x,t)$ denotes the actual evolution given by the data, the evolution of the parameters will be determined in the 'most optimal way', i.e. by determining $p(t)$ such that it minimizes the difference with the actual signal:

$$\min\left\{ \int_{\mathcal{T}} \left\| S(x,t) - \zeta\big(p(t)\big)(x) \right\|^2 \mathrm{d}t \;\middle|\; p \right\}. \tag{1}$$

* Correspondence and reprints.
E-mail address: wilbert.ijzerman@philips.com (W.L. IJzerman).

In this way the signal S is approximated as good as possible by a trajectory in $\mathcal{PM}$:

$$t \to \zeta\big(\hat{p}(t)\big)(x) \in \mathcal{PM}. \tag{2}$$

This best approximation, the projection in the manifold, is called the $\mathcal{PM}$ approximation. Having defined the spatial structures by the choice of the manifold, the parameter dynamics gives additional physical information about the signal.

For the mixing layer to be considered, we investigate two choices for the manifold. One of the $\mathcal{PM}$s is based on a relatively simple description of the vortices. Models that are used to describe vorticial behavior in flows are often based on simple analytical expressions for these structures such as point-vortices, [1], elliptical vortex patches, [2] or Lamb-vortices, [3]. However, comparing the point-vortices and elliptical vortex patches with the data from direct numerical simulations shows that these analytical vortices do not resemble the numerical vortices very closely. In the case where the Reynolds number is not too large, a much better resemblance is obtained with Lamb-vortices, in particular when these circular symmetric vortices are modified to Gaussian profiles with elliptical contour lines as proposed by Ting and Klein, [3]. Therefore such more general vortices will be used to construct the first model manifold. The second manifold is an extension of the first manifold; now the vortices are described by an optimal spatial structure instead of the Gaussian profiles.

In section 2 we discuss the temporal mixing layer, the numerical simulation of this system and we show the spiraling behavior and the merging of the vortices. For this phenomenon we construct the two phenomenological model manifolds in detail in section 3. In section 4 the results of the $\mathcal{PM}$ analysis for the merging of two vortices are presented. The quality of and the physics corresponding to the approximation, as well as the predicted shape of the vortices are discussed. In section 5 we analyze the successive pairwise merging of four vortices. The trajectories of the vortices and the corresponding time-scales are considered. In the final section 6, some conclusions and remarks are given.

2. The two-dimensional temporal mixing layer

In Computational Fluid Dynamics the temporal mixing layer is often used as a model to investigate coherent structures that are also observed in more general and complex systems, see for example [6,10,7–9,5,4,12,11]. A spatial mixing layer can be observed behind a splitter plate, where two fluids with different velocities merge together. This system is convectively unstable due to the Kelvin–Helmholtz instability, see Batchelor, [13]. Fluctuations will grow, and vortices appear, [14]. These vortices will merge, break up and finally evolve into a turbulent flow (when the viscosity is small enough).

The temporal mixing layer is a simplification of the spatial mixing layer. It consists of a box with periodic boundary conditions in the x-direction and free-slip boundary conditions in the y-direction. The upper- and lower-boundaries are taken far away (in the numerical calculations it was verified that they do not influence the dynamics of the system).

For the temporal mixing layer the full Navier–Stokes equations were solved using a fourth-order finite difference scheme in space and a low storage four stage second-order Runge Kutta method for the time integration; see Vreman [12,11] for a similar approach. The Reynolds number $Re = U\delta_i/\nu$ was 100, based on the vorticity thickness δ_i of the initial profile where U and ν are reference velocity and viscosity. The Mach number was chosen small, $M = 0.02$; the system behaves much like an incompressible fluid.

All computations were performed for a domain: $\mathcal{D} = [-L_x, L_x] \times [-L_y, L_y]$ with $L_x = 5\pi$ and $L_y = 20$ ($L_x = 10\pi$, $L_y = 30$ for four vortices) with 128 intervals in the x- and y-direction (256 for four vortices). It

was found that point-wise differences of computations on a 128^2 and 256^2 grid are of the order of 0.5% after 100 units of time, which is considered to be negligible.

In the following we use the vorticity $\omega = \partial_x v - \partial_y u$ to describe the $\mathcal{PM}$. Alternatively, we could also have used the pressure as a quantity to describe the structures.

In the numerical simulation we use as initial conditions a tanh-profile for the x-component of the velocity, $u = \tanh(y)$, a vanishing y-component, $v = 0$, and a constant pressure, $P = 1$. This velocity profile is an approximation of the profile behind a splitter plate, see Monkewitz and Huerre, [15]. To initiate the formation and merging of vortices we use the most unstable disturbance according to the linear stability theory which has wavelength $2\pi/\alpha$ with $\alpha = 0.4$, [19,15,17,18,16]. When the length of the domain is twice as long, two vortices are formed. An additional disturbance with wavelength $4\pi/\alpha$ forces these vortices to merge, see IJzerman for the details, [20]. When the length of the domain is four times as long, four vortices are formed. With the two disturbances mentioned above the vortices will merge pairwise; an additional disturbance with wavelength $8\pi/\alpha$ forces these newly formed vortices to merge to one large vortex.

To study the applicability of the $\mathcal{PM}$ method we first consider the merging of two vortices. In this analysis the amplitude of both disturbances is taken to be 0.01. Then we also analyze the successive pairwise merging of four vortices, for which the amplitudes are taken to be 0.01, 0.001 and 0.0001 for the disturbances with wavelength $2\pi/\alpha, 4\pi/\alpha$ and $8\pi/\alpha$ respectively.

The subsequent evolution of the initial situation corresponding to the merging of two vortices is shown in *figure 1*. The evolution of four vortices will be discussed in section 6. In the first two pictures, $t = 10, 20,$

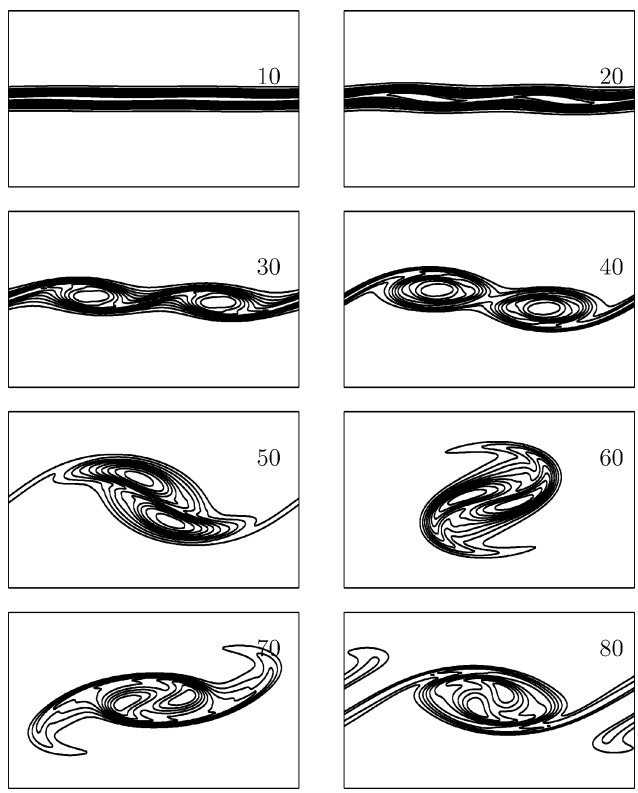

Figure 1. The results of a DNS of the two-dimensional temporal mixing layer. The contour lines show the vorticity at $t = 10, 20, 30, 40, 50, 60, 70$ and 80.

we see primarily the growth of the most unstable mode: Kelvin–Helmholtz instability grows and non-linearity takes over. Two vortices are formed at one and three quarters of the domain, visible at $t = 30$. Attached to these vortices are spiral arms which are wrapped around the core. Due to the additional disturbance with wavelength $4\pi/\alpha$ the vortices have a mutual interaction that causes them to spiral around each other, visible at $t = 40, 50$. Gradually they merge into one large vortex in the middle of the domain, shown at $t = 60, 70$. Viscosity will cause this large vortex to broaden and gradually to disappear (see $t = 80$). For very large times we are left with a profile that is uniform in the x-direction (not shown).

3. Construction of $\mathcal{PM}$ for the mixing layer

In this section two $\mathcal{PM}$s will be constructed for the analysis of the spiraling behavior and the merging of two vortices. In the construction of the model manifold two properties of the computational domain have to be taken into account. Firstly the computational domain is periodic in the x-direction; to construct a manifold which is periodic in this direction the method of images will be used. Secondly the phenomenon is point symmetric with respect to the origin: $\omega(x, t) = \omega(-x, t)$, which makes it possible to describe only one of the two vortices that are visible in the computational domain.

Before presenting the details, we first make a simplification inspired by the physical problem under consideration.

3.1. Amplitude as a special parameter

In the introduction, the parameters were collectively denoted by p. For the specific example to be treated here, it is simpler to specify one parameter that measures the strength of the phenomenon, an amplitude parameter ψ. Then the original minimization problem turns into a reduced maximization problem, as we shall now show.

Denoting the amplitude by ψ and the remaining parameters by p, an element $\zeta(p, \psi)(x)$ in the manifold is written as:

$$\zeta(p, \psi)(x) = \psi\Phi(p)(x), \tag{3}$$

where $\Phi(p)(x)$ denotes the spatial structure. In order to define the amplitude ψ uniquely, the norm of the function Φ has to be prescribed, which will be assumed in the following without explicit reference to simplify the expressions. For spatial structures of the form (3) the minimization problem (1) reads:

$$\min\left\{ \int_{\mathcal{T}} \left\| S(x, t) - \psi(t)\Phi\big(p(t)\big)(x) \right\|^2 \mathrm{d}t \;\middle|\; p, \psi \right\}. \tag{4}$$

Taking the variational derivative with respect to ψ and equate it to zero results in:

$$\psi(t) = \frac{\langle S, \Phi \rangle}{\langle \Phi, \Phi \rangle}, \tag{5}$$

where $\langle S, \Phi \rangle$ denotes the L^2-inner product over the spatial coordinates:

$$\langle S, \Phi \rangle \equiv \big\langle S(x, t), \Phi\big(p(t)\big)(x) \big\rangle;$$

in the same way $\langle \Phi, \Phi \rangle$ denotes the norm of the spatial structure $\Phi(p(t))(x)$. Substituting the relation (5) in (4) results in the maximization problem:

$$\max\left\{ \int_{\mathcal{T}} \frac{\langle S, \Phi \rangle^2}{\langle \Phi, \Phi \rangle} \, \mathrm{d}t \;\middle|\; p \right\}. \tag{6}$$

Observe that for this problem the functional is bounded from above, due to the Cauchy–Schwarz inequality:

$$\int_{\mathcal{T}} \frac{\langle S, \Phi \rangle^2}{\langle \Phi, \Phi \rangle} \, \mathrm{d}t \leqslant \int_{\mathcal{T}} \langle S, S \rangle \, \mathrm{d}t = \int_{\mathcal{T}} \left\| S(x,t) \right\|^2 \mathrm{d}t$$

and that equality is obtained only when $\Phi \equiv \Phi(p(t))(x)$ is a multiple of $S(x,t)$.

The right-hand side of the above inequality is interpreted as the total 'energy' in the signal. In this paper $S = \omega$, and hence the energy is enstrophy here. The value of (6) divided by the total energy therefore denotes the fraction of the total energy captured by Φ in the $\mathcal{PM}$ approximation. This fraction, ρ, is a measure of the quality of the approximation because it is related to the relative error ε in the following way:

$$\varepsilon = \frac{\int_{\mathcal{T}} \| S(x,t) - \hat{\psi}(t)\hat{\Phi}(x) \|^2 \, \mathrm{d}t}{\int_{\mathcal{T}} \| S(x,t) \|^2 \, \mathrm{d}t} = 1 - \rho,$$

where $\hat{\psi}$ and $\hat{\Phi}(x) \equiv \Phi(\hat{p}(t))(x)$ denote the optimal amplitude and spatial structure corresponding to the solution of the maximization problem (6).

4. $\mathcal{PM}$ with elliptical Gaussian vortices

Flow visualization suggest that the coherent structures are approximately Gaussian profiles, see, e.g., *figure 2*. Circular profiles known as Lamb vortices were used by [3] to model the merging of two vortices. The contourlines in *figures 1* and *2* show, however, that the vortices are more elliptical than circular. Therefore each vortex is approximated by a Gaussian profile with elliptical contourlines. In doing so, the model manifold

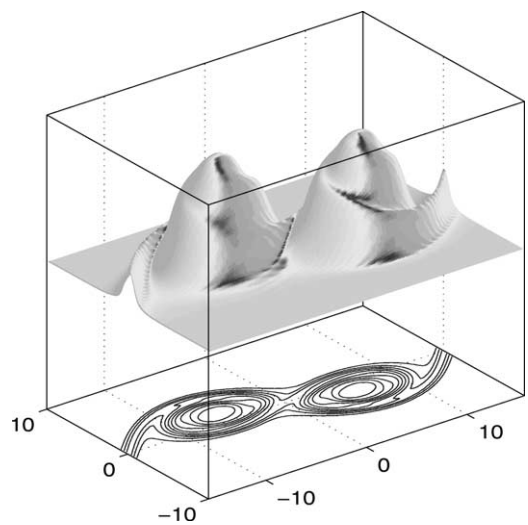

Figure 2. A surface plot com and corresponding contourplot of the vorticity at $t = 40$. This figure motivates the choice of Gaussian vortices with elliptical contour lines in the model manifold $\mathcal{PM}_{\text{Gauss}}$.

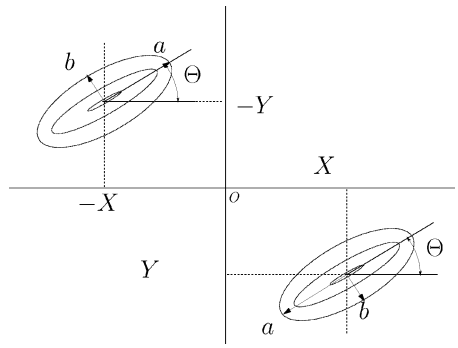

Figure 3. In this figure the parameters X, Y, Θ, a and b which are used to describe the vortices in the $\mathcal{PM}$s are shown.

contains as parameters the position of the vortex, X, Y, the orientation Θ, which is defined with respect to a fixed coordinate system, and the length of the main axes a, b, see *figure 3*. Every vortex is then approximated by a spatial structure:

$$G(x, y) = \exp\left(-\frac{1}{2}\left(\frac{X_\Theta(x, y)}{a}\right)^2 - \frac{1}{2}\left(\frac{Y_\Theta(x, y)}{b}\right)^2\right) \tag{7}$$

in which

$$X_\Theta(x, y) = (x - X)\cos(\Theta) + (y - Y)\sin(\Theta),$$
$$Y_\Theta(x, y) = -(x - X)\sin(\Theta) + (y - Y)\cos(\Theta).$$

Taking periodicity and point symmetry into account, the model manifold has the form:

$$\mathcal{PM}_{\text{Gauss}} = \left\{ \psi \sum_{k=-\infty}^{\infty} G(x + 2k\,L_x, y) + G(2k\,L_x - x, -y) \;\middle|\; p, \psi \right\},$$

where p denotes the parameters (X, Y, Θ, a, b), ψ is the amplitude and the sum over k relates to the use of the method of images.

4.1. $\mathcal{PM}$ with optimised spatial structure

Since the choice of a Gaussian profile for the vortices may be too restrictive, we also investigate an extension of the above manifold. In this extension the Gaussian profile, (7), is replaced by a spatial structure, ϕ:

$$G_{\text{Opti}}(x, y) = \phi\left(\frac{X_\Theta(x, y)}{a}, \frac{Y_\Theta(x, y)}{b}\right). \tag{8}$$

This spatial structure ϕ is chosen optimal, and so the model manifold is extended to a manifold with an additional free function:

$$\mathcal{PM}_{\text{Opti}} = \left\{ \psi \sum_{k=-\infty}^{\infty} G_{\text{Opti}}(x + 2k\,L_x, y) + G_{\text{Opti}}(2k\,L_x - x, -y) \;\middle|\; \phi, p, \psi \right\}. \tag{9}$$

In the following we will specify how the function ϕ is optimised in the numerical scheme.

4.1.1. Numerical solution of the optimization problem

We first apply the $\mathcal{PM}$ analysis to the spiraling behavior and the merging of two vortices in the interval $t \in [20, 60]$. The snapshots of the data are taken at equidistant moments in time with $\Delta t = 0.2$ or 0.4, thus the number of snapshots, denoted by N_T, equals 201 or 101 respectively.

For the numerical solution of the optimization problem (6) we have to discretize the problem. The parameters are only determined at the equidistant instants t_j, $j = 1, \ldots, N_T$, at which the signal S is known. We denote the parameters at these instants t_j by p_j.

The free function ϕ in $\mathcal{PM}_{\text{Opti}}$ was described by a finite set of N^2 base functions, $\xi_k(x)\xi_l(y)$, $k, l = 1, 2, \ldots, N$. When the coefficients of ϕ with respect to the base functions are denoted by c_{kl} we have:

$$\phi(x, y) = \sum_{k,l=1}^{N} c_{kl}\xi_k(x)\xi_l(y).$$

The base functions were chosen such that for $N = 1$, $\mathcal{PM}_{\text{Opti}}$ corresponds to $\mathcal{PM}_{\text{Gauss}}$, i.e. ξ_1 is a Gaussian profile. Orthogonal functions for which the first element corresponds to a Gaussian profile are the Gauss–Hermite polynomials given by:

$$\xi_m(x) = H_m(x)\exp\bigl(-x^2/2\bigr),$$

for $m = 1, 2, \ldots$ with

$$H_1 = 1, \qquad H_2 = 2x, \quad \text{and} \quad H_k(x) = 2x\,H_{k-1}(x) - 2(k-2)\,H_{k-2}(x)$$

for $k = 3, 4, \ldots$.

Denoting the manifold based on N^2 base functions by $\mathcal{PM}_{\text{Opti}}(N)$, a larger number of base functions leads to a larger manifold:

$$\mathcal{PM}_{\text{Opti}}(N') \subset \mathcal{PM}_{\text{Opti}}(N) \quad \text{for } N' \leqslant N. \tag{10}$$

As a consequence, the fraction of the total energy captured by an approximation in $\mathcal{PM}_{\text{Opti}}(N)$ is larger than the fraction for $\mathcal{PM}_{\text{Opti}}(N')$. In particular, an approximation in $\mathcal{PM}_{\text{Gauss}}$ $(N = 1)$ contains less energy than an approximation in $\mathcal{PM}_{\text{Opti}}(N)$, $N > 1$.

Using the base functions ξ_k, $k = 1, 2, \ldots, N$, an element $\zeta(p, \psi, \phi)(x)$ in $\mathcal{PM}_{\text{Opti}}$ can be written as:

$$\zeta(p, \psi, \phi)(x, y) = \psi \sum_{k,l=1}^{N} c_{kl}\,\Xi_{kl}(p)(x, y),$$

where

$$\begin{aligned}\Xi_{kl}(p)(x, y) = \sum_{p=-N_s}^{N_s} &\xi_k\left(\frac{X_\Theta(x + 2p\,L_x, y)}{a}\right)\xi_l\left(\frac{Y_\Theta(x + 2p\,L_x, y)}{b}\right)\\ &+ \xi_k\left(\frac{X_\Theta(-x + 2p\,L_x, -y)}{a}\right)\xi_l\left(\frac{Y_\Theta(-x + 2p\,L_x, -y)}{b}\right).\end{aligned}$$

In this expression the infinite sum in (9) is replaced by a finite sum over N_s elements. Since the base functions fall off to zero quickly a value of 1 for N_s turned out to be sufficient. Increasing N_s did not influence the fraction of the energy captured by the approximation.

Using the following abbreviations: $D^j_{kl} = \langle S(x,t_j), \Xi_{kl}(p_j)(x,y)\rangle$, $M^j_{klmn} = \langle \Xi_{kl}(p_j)(x,y), \Xi_{mn}(p_j)(x,y)\rangle$ for $j = 1, 2, \ldots, N_T$, the optimization problem (6) can be written as:

$$\max\left\{ \frac{(\sum_{k,l} D^j_{kl} c_{kl})^2}{\sum_{k,l,m,n} M^j_{klmn} c_{kl} c_{mn}} w_j \;\middle|\; p_j, c_{kl} \right\}. \tag{11}$$

For all spatial and temporal integrations which occur in the above expressions the trapezoidal rule was used. For the temporal integration the weight factors take: $w_j = \Delta t$, $j = 2, \ldots, N_T - 1$, and $w_1 = w_{N_T} = 1/2\Delta t$, where Δt is the length of the snapshot interval.

The optimization problem (11) is solved iteratively using a variant of the relaxation method, see Ciarlet, [21]. Every iteration consists of two steps. In the first step the best parameter vector p_j is obtained at every instant:

$$\max\left\{ \frac{(\sum_{k,l} D^j_{kl} c_{kl})^2}{\sum_{k,l,m,n} M^j_{klmn} c_{kl} c_{mn}} \;\middle|\; p_j \right\}, \quad \text{for } j = 1, 2, \ldots, N_T$$

while the coefficients c_j are fixed at the value of the previous iteration. Because the functions Ξ_{kl} depend in a complicated way on the parameters, the calculation of the derivatives to the parameters is a time consuming task. To avoid their calculation, the above optimisation problem is solved using a Newton method in which finite difference estimates are used for the derivatives.

In the second step of the iteration the best spatial structure is determined for the optimal parameters obtained in the first step. This results in the following optimization problem:

$$\max\left\{ \sum_{j=1}^{N_T} \frac{(\sum_{k,l} D^j_{kl} c_{kl})^2}{\sum_{k,l,m,n} M^j_{klmn} c_{kl} c_{mn}} w_j \;\middle|\; c_{kl} \right\}. \tag{12}$$

For this problem the derivatives to the coefficients are simple and cheap to calculate. Hence a Newton-method suffices to solve this optimization problem.

For $\mathcal{PM}_{\text{Gauss}}$ N equals 1 and the first step of the above iteration process has to be applied only once. The value of the quotient in (12) for $N = 1$ is independent of c_{11} and the optimal parameter vectors p_j, $j = 1, \ldots, N_T$, are determined by applying the first step.

5. $\mathcal{PM}$-analysis of the vortex merging

In this section we discuss the results obtained in the $\mathcal{PM}$ analysis using the two manifolds constructed in the previous section. All results were obtained with $N_T = 201$ and $N = 15$. As we will show later on, changing the number of snapshots, N_T, and the number of base functions N^2 does not significantly change the fraction of energy captured by the $\mathcal{PM}$ approximations. Hence these numbers were considered to be sufficient.

5.1. Reconstruction of the signal

The signal itself and the $\mathcal{PM}$ approximations in both manifolds, $\mathcal{PM}_{\text{Opti}}$ and $\mathcal{PM}_{\text{Gauss}}$ are shown in ***figure 4***. At $t = 28, 36, 44$ and 52 the approximations have two vortices at approximately the same position and with the same orientation as in the DNS signal. At $t = 60$ the $\mathcal{PM}$ approximations show two humps of vorticity which are at different positions and have different orientations. The signal shows one large vortex in the middle of the

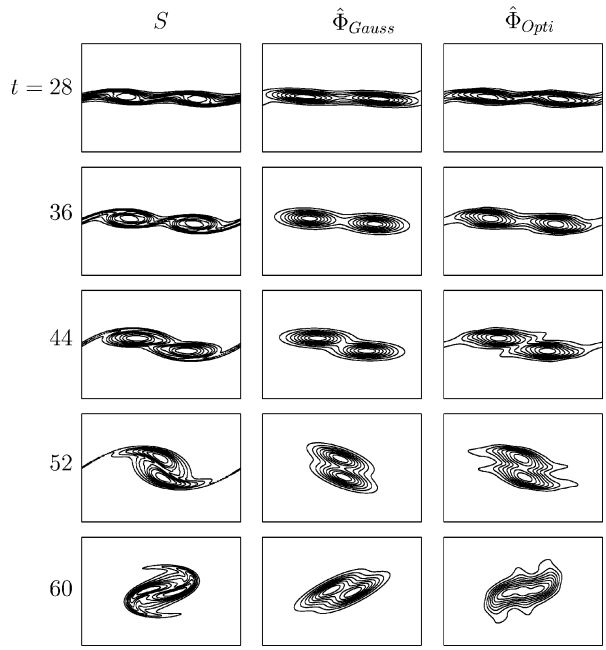

Figure 4. In the first column the signal is shown at $t = 28, 36, 44, 52$ and 60. In the second and third column we see the corresponding approximations in $\mathcal{PM}_{\text{Gauss}}$ and $\mathcal{PM}_{\text{Opti}}$ respectively.

domain consisting of two small maxima and spiral arms which are wrapped around the core. In the manifolds this single vortex is approximated by two vortices. So this suggests the use of another type of $\mathcal{PM}$ if one would like to analyze the signal beyond this time.

For both $\mathcal{PM}$ approximations the spiral arms between the vortices are not well represented. This is to be expected for $\mathcal{PM}_{\text{Gauss}}$ since G does not describe such arms at all. For $\mathcal{PM}_{\text{Opti}}$ this may be explained as follows. The main part of the vorticity is in the core of the vortices and these cores move along a different trajectory than the spiral arms do. To capture the largest fraction of the energy the trajectory, $(X(t), Y(t))$, obtained in the $\mathcal{PM}$ analysis, follows the core of the vortices. Thus the spiral arms are effectively removed in the time averaging of (6) and the $\mathcal{PM}$ approximation will not show them.

5.2. Spatial extent of the coherent structures

Contour lines of the spatial structures G, (7) and $\hat{G}_{\text{Opti}}$, (8) are shown in *figure 5*. Both structures are placed at the origin $X = 0,\ Y = 0$, and their main axes coincide with the coordinate system, $\Theta = 0$. These main axes, a, b, are given the value at the beginning of the time-interval, $t = 20$. Although the structures are defined on the whole $\mathbb{R}^2$, the domain shown in the figure is just the computational domain. The spatial structures resemble each other. This explains why both $\mathcal{PM}$ approximations are of the same quality as we will see later on.

5.3. Dynamics of the parameters

The position of one of the two vortices in the computational domain (*figure 1*) and the corresponding trajectories of both vortices are shown in *figures 6*(*a*) and *7* respectively. The trajectories clearly show the spiraling behavior of the vortices. When the vortices are well separated the trajectories of both approximations

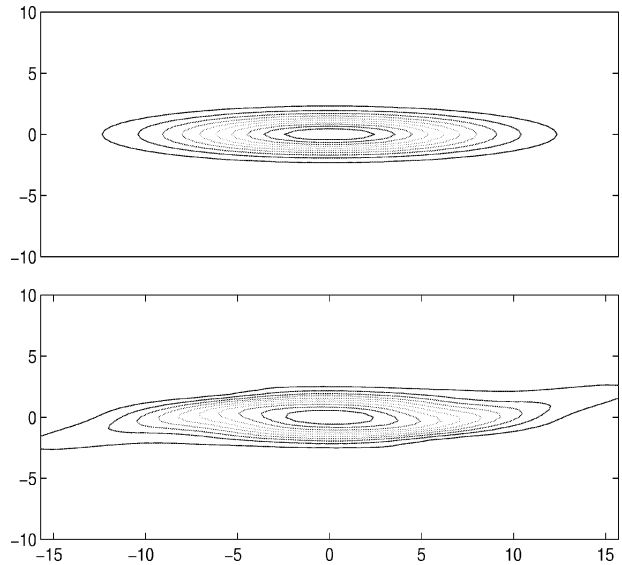

Figure 5. Contour lines of the vorticity for the structures G (top) and G_{Opti} (bottom) obtained in the $\mathcal{PM}$ analysis. The structures are placed in the origin and the main axes have the values of the beginning of the time-interval.

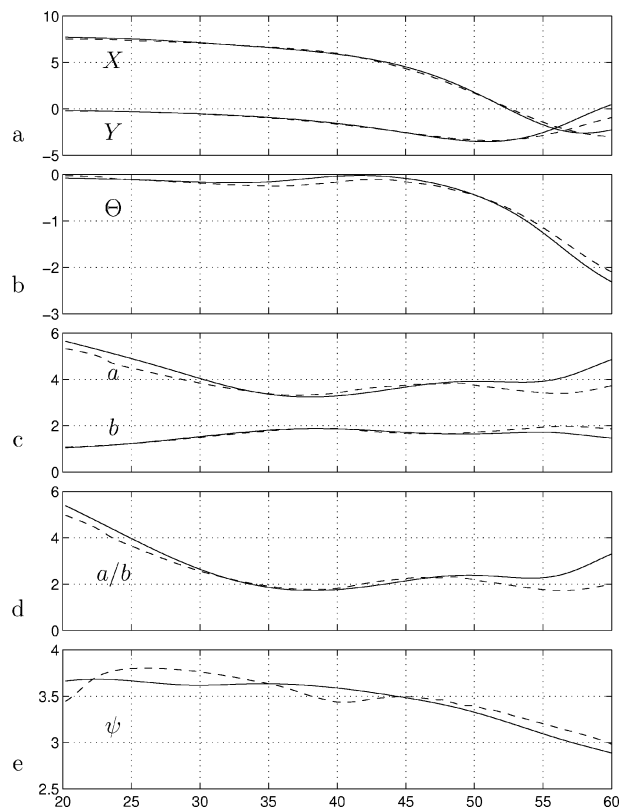

Figure 6. In this figure we see from top down the values of the parameters X, Y, Θ, a and b, ellipticity a/b and ψ as a function of time. The results with $\mathcal{PM}_{\mathrm{Opti}}$ are denoted dashed lines and the results with $\mathcal{PM}_{\mathrm{Gauss}}$ by solid lines.

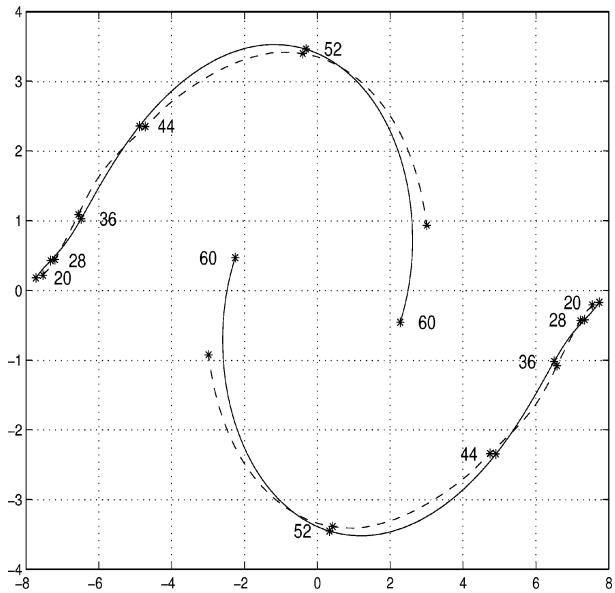

Figure 7. The trajectories of the vortices obtained in the $\mathcal{PM}$ analysis using $\mathcal{PM}_{\text{Gauss}}$ (solid line) and $\mathcal{PM}_{\text{Opti}}$ (dashed line). The markers in this figure show the position of the vortices at $t = 20, 28, 36, 44, 52$ and 60.

resemble each other. At the end of the time-interval when the vortices have almost merged, differences in the trajectories occur. The approximation in $\mathcal{PM}_{\text{Gauss}}$ results in vortices which rotate around each other over a larger angle.

The orientation of the vortices, Θ, which was defined with respect to a fixed coordinate system (*figure 3*), is shown in *figure 6*(b) as a function of time. At $t = 20$ the vortices are oriented along the x-axis, but when they spiral around each other, the main axes approximately coincides with the tangent at the trajectory. Hence the orientation increases at the beginning, when the vortices have just started moving. In the rest of the time-interval the vortices spiral around each other and the orientation decreases.

The main axes, a, b, and the corresponding ellipticity, a/b, are shown in *figures 6*(c) and *6*(d) respectively. At $t = 20$ the vorticity in the DNS data is primarily found along the x-axis. As a result, the vortices in the $\mathcal{PM}$ approximations are stretched along this axis and have a large ellipticity. The ellipticity decreases when the vortices start moving. At the end of the time-interval the DNS data shows one vortex in the middle of the computational domain. Because this single vortex is in the $\mathcal{PM}$ analysis approximated by two elliptical vortices lying along each other the ellipticity in this representation increases again.

The amplitudes ψ for both $\mathcal{PM}$ approximations which are given by the relation (5) are shown in *figure 6*(e). To construct this figure the structures G and G_{Opti} were normalized such that $\|G\| = \|G_{\text{Opti}}\| = 1$ at $t = 20$. For both $\mathcal{PM}$ approximations the amplitudes are mainly decreasing. This is the result of interplay between decrease due to viscosity which reduces the maximal vorticity in the DNS data and decrease because the vortices approach each other and the vorticity in the flank of one vortex is added to the vorticity in the core of the other.

5.4. Discretization errors

In the $\mathcal{PM}$ analysis using $\mathcal{PM}_{\text{Opti}}$ and $\mathcal{PM}_{\text{Gauss}}$ two types of discretization errors occur. We have errors due to the finite number (N^2) of base functions in $\mathcal{PM}_{\text{Opti}}$ and due to the finite number of snapshots (N_T) in

Table I. The fraction of the total energy captured by the $\mathcal{PM}$ approximation using several values of N and N_T. The column with $N = 1$ corresponds to $\mathcal{PM}_{\text{Gauss}}$.

N	1	5	10	15
$N_T = 101, \Delta t = 0.4$	0.9573	–	–	0.9717
$N_T = 201, \Delta t = 0.2$	0.9571	0.9675	0.9704	0.9715

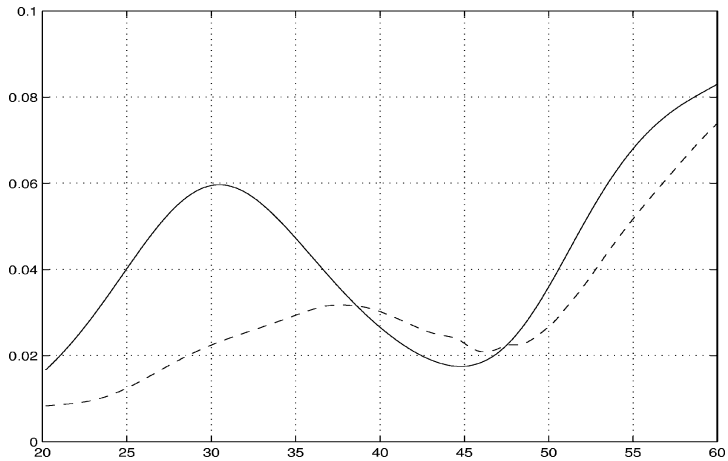

Figure 8. The relative error (13) for the $\mathcal{PM}$ analysis using $\mathcal{PM}_{\text{Gauss}}$ (solid line) and $\mathcal{PM}_{\text{Opti}}$ (dashed line).

the time-interval. The effect of these errors was investigated by varying N and N_T and considering the fraction of the total energy captured by the corresponding $\mathcal{PM}$ approximations. These fractions are collected in *table I*.

The fractions in the table are increasing functions of N, in correspondence with relation (10). The differences between $N = 10$ and 15 are less than 0.11% and considered to be negligible. We remark that ρ does not converge to 1 if N increases to ∞, since it is not necessary that we can describe the whole dynamics of S by our model manifolds.

For two different numbers of snapshots $N_T = 101$ and 201 the fractions of energy are also shown in *table I*. For $\mathcal{PM}_{\text{Gauss}}$ as well as $\mathcal{PM}_{\text{Opti}}(15)$ the differences are less than 0.02%. Hence we consider the time-integration to be sufficiently converged. We considered the numerical results for $N = 15$ and $N_T = 201$ only.

5.5. Relative errors

A measure for the quality of the approximation at each instant is given by the following relative error:

$$\varepsilon(t) = \frac{\|S(x,t) - \hat{\psi}(t)\hat{\Phi}(x)\|^2}{\|S(x,t)\|^2}, \tag{13}$$

where $\hat{\psi}$ and $\hat{\Phi}(x) \equiv \Phi(\hat{p}(t))(x)$ denote the optimal amplitude and spatial structure corresponding to the solution of the maximization problem (6).

For both $\mathcal{PM}$ approximations this relative error is shown in *figure 8*. In the first and last part of the time-interval $\mathcal{PM}_{\text{Opti}}$ gives better approximations than $\mathcal{PM}_{\text{Gauss}}$, but for all instants the errors are of a

comparable size. The increasing error at the end of the time-interval corresponds to the discrepancy between the reconstruction of the signal and the DNS signal at $t = 60$ as shown in *figure 4*.

Because the fraction of the energy is an increasing function of N, the $\mathcal{PM}$ approximation in $\mathcal{PM}_{\text{Gauss}}$, $(N = 1)$ contains less energy than the approximation in $\mathcal{PM}_{\text{Opti}}(15)$. However, this does not imply that the relative error is smaller at every instant as shown, e.g., in the interval [40, 45].

6. Successive pairwise merging of four vortices

In this section we study the successive pairwise spiraling and merging of four vortices using model manifolds based on Gaussian profiles. As described in section 2, four vortices are formed in a computational domain which is twice as long as the domain used in the analysis of the previous section. The subsequent evolution of such a system, for initial conditions as described in section 2, is shown in *figure 9*. At $t = 20, 30$ we see the formation of four vortices at one, three, five and seven eighths of the domain. The disturbance with wavelength $4\pi/\alpha$ causes these vortices to spiral and merge pairwise to the two vortices visible at one and three quarters of the domain, $t = 100$ and 160. Due to the extra disturbance with wavelength $8\pi/\alpha$, these newly formed vortices spiral and merge again to one large vortex in the middle of the domain, visible at $t = 240$.

In the evolution of the four vortices we can distinguish two stages which have to be analyzed separately. In the first stage, which occurs approximately in the time interval [20, 100], the four vortices merge pairwise to form two vortices. In the second stage, approximately at [100, 220] the two newly formed vortices merge to one large

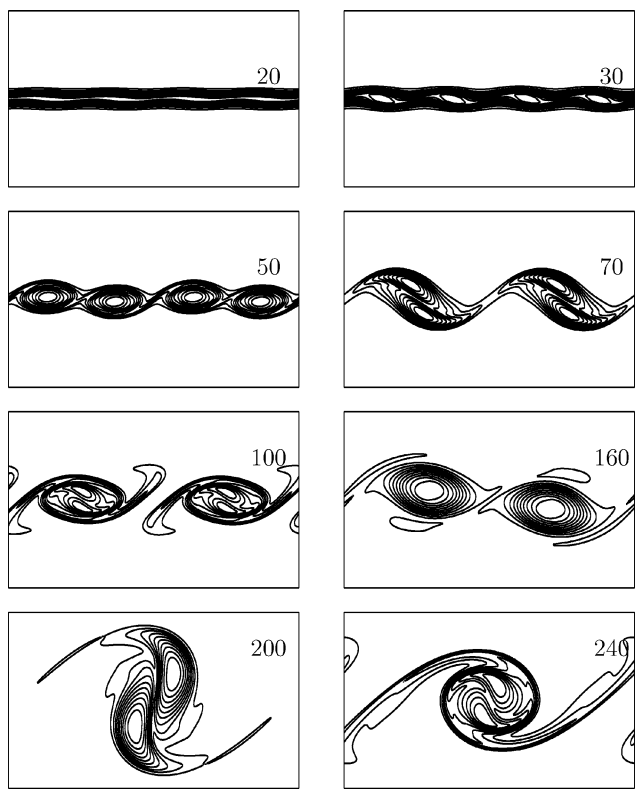

Figure 9. The results of a DNS of the two-dimensional temporal mixing layer for a computational domain which is twice as long as the domain in *figure 1*. The contour lines show the vorticity at $t = 20, 30, 50, 70, 100, 160, 200$ and 240.

vortex. For the analysis of the second stage the model manifold $\mathcal{PM}_{\text{Gauss}}$, which was designed in section 3, is used. For the first stage a model manifold is used which is an extension of this model manifold; instead of one Gaussian profile described by six parameters two Gaussian profiles described by twelve parameters are used, together with the method of images and the point symmetry, to describe the four observed coherent structures.

For both stages the trajectories obtained in the $\mathcal{PM}$ analysis are shown in *figure 10*. The trajectories in the computational domain, *figure 10*(*a*), show for both stages the spiraling behavior of the vortices. The trajectory in the second stage is more than two times larger than the trajectory in the first stage. The x- and y-coordinates

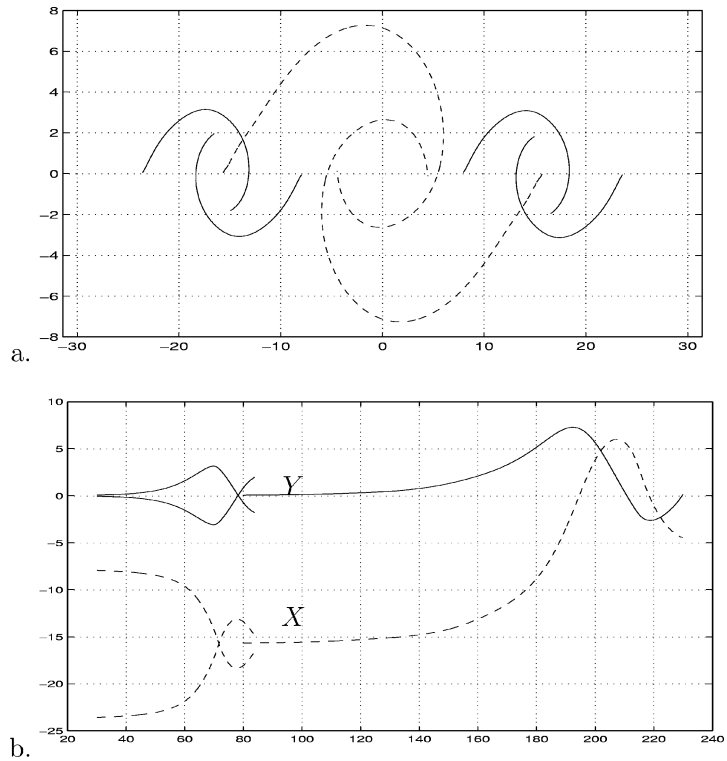

Figure 10. In (a) we see the trajectories obtained in the $\mathcal{PM}$ analysis of the four vortices shown in *figure 9*. The trajectories of the four vortices in the first stage are denoted by the solid lines and for the second stage by dashed lines. In (b) we see the x- (dashed lines) and y-coordinates (solid lines) as functions of time. Only the trajectories of the vortices which started in the left side of the computational domain are shown.

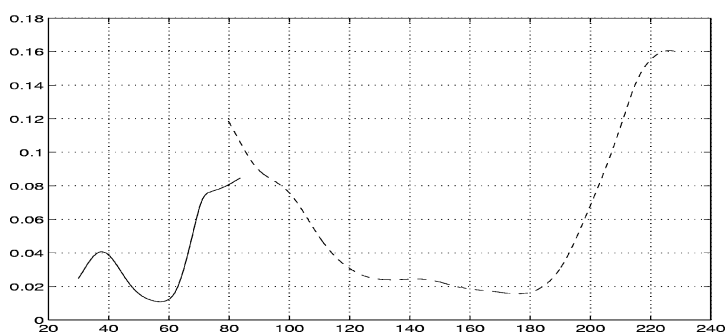

Figure 11. This figure shows the relative error for the first stage (solid line) and the second stage (dashed line).

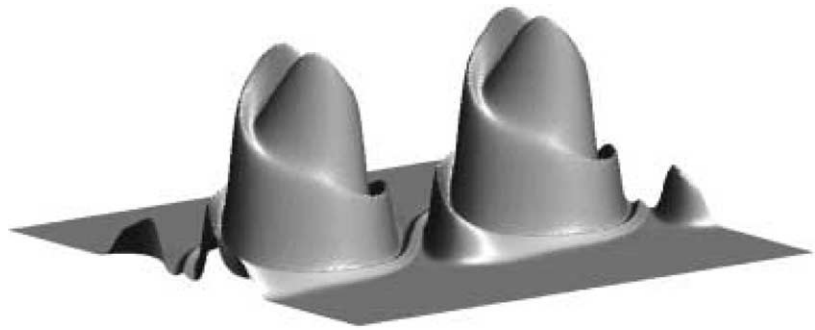

(a)

(b)

Figure 12. In (a) we see a surface plot of the vorticity at the end of the first stage, $t = 100$, and in (b) at the end of the second stage, $t = 220$. The figures show that the vorticity distribution between the first stage and at the end of the second stage is quite complicated and cannot be well approximated by a Gaussian profile.

of the vortices as function of time are shown in *figure 10*(*b*). We see that the spiraling behavior occurs in the first stage at a much smaller time scale than in the second stage.

For both stages the relative errors (13) are shown in *figure 11*. When the vortices are well separated the relative errors are small and when the vortices approach each other the error increases. At the end of the first, $t \approx 100$, and second stage, $t \approx 220$, the vorticity distribution becomes very complicated, see *figure 12*, and cannot be approximated by four and two Gaussian profiles respectively. Just as in the previous section, in which we could not analysis the signal beyond $t = 60$, this suggests the use of another type of manifold to analyze these parts of the evolution.

To quantify the time scales at which the above described mergings occur we proceed as follows. We define a characteristic time as the time which elapses between the instant at which the trajectory crosses the y-axis and the first instant at which the trajectory crosses the x-axis, or stated otherwise, the characteristic time is the time that elapses between the instant at which the vortices are aligned vertically and horizontally, see *figure 13*. For vortices that rotate with a fixed angular velocity around each other, this time scale corresponds to a quarter of the period. It is possible to define a different time scale, but we do not believe that for a different time scale the discussion below would change in a qualitative sense.

Using the characteristic time defined above we obtain the following time scales for the trajectories of the vortices obtained in the $\mathcal{PM}$ analysis and presented in *figure 10*. For the first merging the trajectory crosses the y-axis at $t \approx 70$ (for all four vortices) while for the second merging this occurs at $t \approx 194$, see *figure 10*.

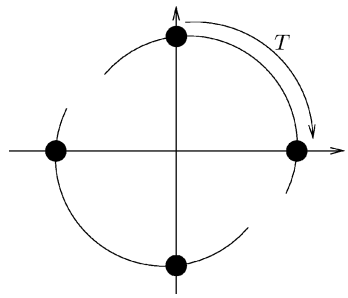

Figure 13. An illustration of the definition of a characteristic time used to quantify the time scales.

The four vortices in the first merging cross the x-axis at $t \approx 78$ and the two vortices in the second merging at $t \approx 210$. Based on these instants the second merging proceeds ≈ 2.11 times slower than the first.

Using a scaling argument we show that the second merging would proceed precisely two times slower than the first if the flow is inviscid and if the initial conditions for the second merging are the scaled initial conditions for the first merging (which we will explain now). The scaling argument is based on the following observation. Suppose we have a solution of the inviscid equations of motion:

$$\partial_t \omega(\mathbf{x}, t) = -\mathbf{u}(\mathbf{x}, t) \cdot \nabla \omega(\mathbf{x}, t) \tag{14}$$

on a domain $x \in [-L, L] \times \mathbb{R}$, which consists of a vorticity and velocity:

$$\omega(\mathbf{x}, t) \quad \text{and} \quad \mathbf{u}(\mathbf{x}, t) \tag{15}$$

respectively with a streamfunction $\Psi(\mathbf{x}, t)$. Then for every $\alpha, \beta \in \mathbb{R}^+$ the following vorticity and velocity:

$$\beta\omega(\alpha\mathbf{x}, \beta t) \quad \text{and} \quad \frac{\beta}{\alpha}\mathbf{u}(\alpha\mathbf{x}, \beta t) \tag{16}$$

with streamfunction $\beta\Psi(\alpha\mathbf{x}, \beta t)/\alpha^2$ are a solution of the equations of motion on $\mathbf{x} \in \mathcal{D}_\alpha = [-L/\alpha, L/\alpha] \times \mathbb{R}$ (which is verified by a substitution of (16) into (14)). For the mixing layer the parameter β is determined by the boundary condition at $y = \pm\infty$, i.e. we have $\mathbf{u} = (\pm 1, 0)$ for $y \to \pm\infty$ and, consequently, $\beta = \alpha$.

The above scaling argument results in a factor two between the time scales of the first and second merging. The first merging occurs in the left and right half of the computational domain, see *figure 9*. Let us consider the merging in the left half only and suppose that the corresponding vorticity (and velocity) is given by (15). The second merging occurs in the whole domain and, so, for this merging the computational domain is twice as large as for the first merging, hence $\alpha = 1/2$. Finally, let us assume that the initial conditions at $t = t_2$ for the second merging are a scaled version of the initial conditions for the first merging at $t = t_1$, i.e:

$$\omega(\mathbf{x}, t_2) = \frac{1}{2}\omega\left(\frac{1}{2}\mathbf{x} + \gamma, t_1\right) \quad \text{or} \quad \mathbf{u}(\mathbf{x}, t_2) = \mathbf{u}\left(\frac{1}{2}\mathbf{x} + \gamma, t_1\right), \tag{17}$$

where $\gamma = (-\frac{1}{2}L_x, 0)$ denotes a shift in the x-direction. Then the relations (16) show that the second merging evolves two times slower than the first.

We assume that the 'initial conditions' for the second merging are a scaled version of the 'initial conditions' for the first merging, to arrive at (17). A priori, the validity of this assumption is disputable. However, the

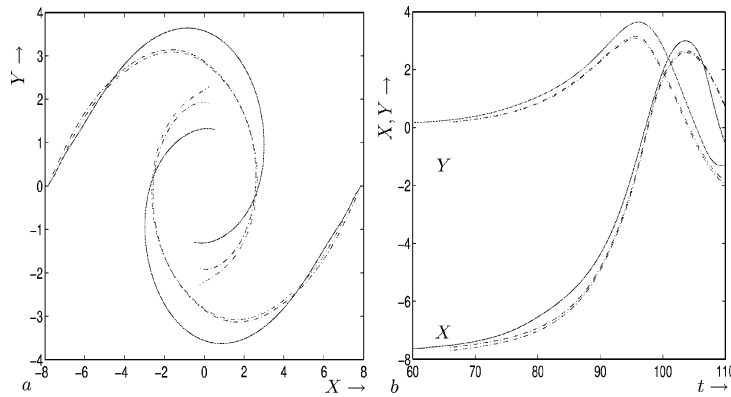

Figure 14. In this figure we compare the trajectories of the vortices obtained in the $\mathcal{PM}$ analysis for the first and second merging where the trajectories for the latter are scaled by a factor two in time and space. In (a) we show the trajectories of the four vortices in the first merging (dash-dotted lines) and the trajectories of the two vortices in the second merging (solid lines). In (b) we observe these trajectories as a function of time.

results of the $\mathcal{PM}$ analysis show that this assumption is approximately satisfied. For instance, in *figure 14* we show the trajectories of vortices for the first and second merging where the latter are scaled by a factor two in space and time, in correspondence with the inviscid scaling law, (17). We observe that the initial positions of the vortices in the first merging nearly coincide with the (scaled) initial position of the vortices in the second merging. *Figure 14* also shows that the second merging evolves more than two times slower than the first. The trajectory, i.e. the amplitude of the spiral, obtained for the second merging is more than two times larger than the two trajectories obtained for the first merging. Initially the trajectories coincide, but for larger times they deviate and if the vortices are vertically aligned the distance between the vortices in the second merging is more than twice the distances between the vortices in the first merging. Under the assumption of scaled initial conditions, the difference between the factor 2.11 and the scaling law factor 2 is a viscous effect. In [20] the influence of the Reynolds number on the time-scales is investigated in detail.

7. Discussion and conclusions

To analyse the merging of vortices in the two-dimensional temporal mixing layer, the signal obtained from a direct numerical simulation was analysed by constructing a parameterised set, the phenomenological model manifold, $\mathcal{PM}$, and the parameters were choosen to depend on time in order to reconstruct the data in an optimal way. The applicability of this method was demonstrated by modelling the successive pairwise merging of four vortices.

Clearly, the actual choice of the manifold is essential for the accuracy of the reconstruction. To investigate this in some detail, we investigated a rather simple, and a more complicated manifold. We briefly describe the results, and relate the presented method to the well known POD-method.

Two model manifolds, $\mathcal{PM}_{\text{Gauss}}$ and $\mathcal{PM}_{\text{Opti}}$, were considered. $\mathcal{PM}_{\text{Gauss}}$ has only six degrees of freedom and is an extension of Ting's model, [3], which uses Lamb vortices with only two degrees of freedom: the positions of the vortices. $\mathcal{PM}_{\text{Opti}}$ allows us to choose the spatial vortices in an optimal way. Both manifolds gave the same qualitative results: the resulting approximations contained approximately the same amount of energy, although the approximation in $\mathcal{PM}_{\text{Opti}}$ contains by construction more energy than the approximation in $\mathcal{PM}_{\text{Gauss}}$. The relative error for both approximations was of a comparable size for the main part of the time-interval. The time-averaged optimal structure G_{Opti} resembled the Gaussian profile and the trajectories,

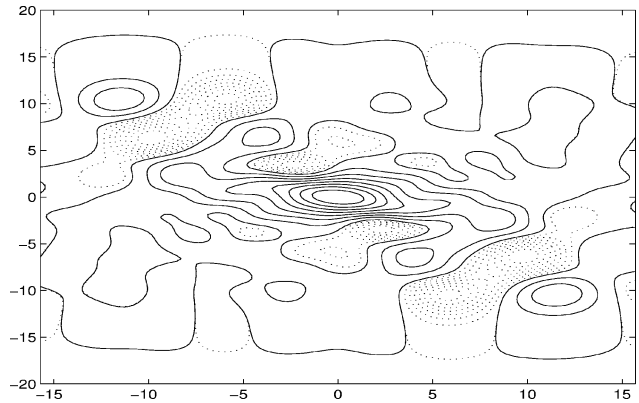

Figure 15. The structure G_{Opti} obtained for an infinitesimal small interval consisting of one instant only ($t = 60$) using N^2, $N = 15$ base functions. The dashed lines denote negative vorticity, the solid lines positive.

orientation and length of the main axes showed the same qualitative behavior. However, the optimization problem for $\mathcal{PM}_{\text{Opti}}$ is much more complicated than the problem for $\mathcal{PM}_{\text{Gauss}}$, because of the larger number of base functions for $\mathcal{PM}_{\text{Opti}}$. For $\mathcal{PM}_{\text{Gauss}}$ less than two and for $\mathcal{PM}_{\text{Opti}}$ approximately 100 hours of computational time were used on a single R10000 processor of a SGI Power Challenge. Because the model manifold $\mathcal{PM}_{\text{Gauss}}$ is much simpler than $\mathcal{PM}_{\text{Opti}}$ and the results obtained in the analysis are qualitatively the same, $\mathcal{PM}_{\text{Gauss}}$ is an efficient, accurate way to provide a low-dimensional model.

We finish with a few additional remarks:

- The spatial structures obtained in $\mathcal{PM}_{\text{Opti}}$ can be completely different from the structure one has in mind during the construction of the model manifold when the time interval in the analysis is short. For example, for the limiting case of a time-interval consisting of one instant only ($t = 60$) the obtained spatial structure is shown in *figure 15*. This optimal structure is not one hump of vorticity, like the structures obtained in the $\mathcal{PM}$ analysis of the interval $[20, 60]$, but it consists of several patches of positive and negative vorticity. It was verified that this structure added to its point-reflected mirror precisely gives the vorticity distribution at $t = 60$; the patches of positive and negative vorticity cancel each other in the summation. It was also observed that for short time-intervals, typically of the order of one unit of time, the obtained spatial structure may consist of several patches of positive and negative vorticity. For these short time-intervals the vortices hardly move with respect to each other and the patches cancel each other in the reconstruction of the signal.
- In the $\mathcal{PM}$ method non-uniqueness of the approximations can occur when the model manifold is not appropriate for the phenomenon. The presented model manifolds were also used in the analysis of the time-interval $[40, 80]$ instead of $[20, 60]$. For the former the parameters show discontinuities. Detailed analysis showed that there exist, at least, two approximations containing the same fraction of the total energy, but with a different position, orientation and spatial extent of the vortices. At the end of the time-interval $[40, 80]$, the two vortices in the DNS data have merged to one large vortex with two small humps of vorticity. Approximating this single vortex by two vortices results in non-uniqueness of the optimum. So the model manifolds were not appropriate for the signal in this interval.
- In the presented method we switch manually from $\mathcal{PM}$ for 4 to $\mathcal{PM}$ for 2 vortices during the merging process. It is possible to automate this step using, e.g., the quantity Q described in [22]. Coherent areas of negative Q can be interpreted as vortices and the position at which Q is (locally) minimal as the eye of the vortex. If two vortices merge, two minima of Q disappear and one new minimum occurs. At this instant

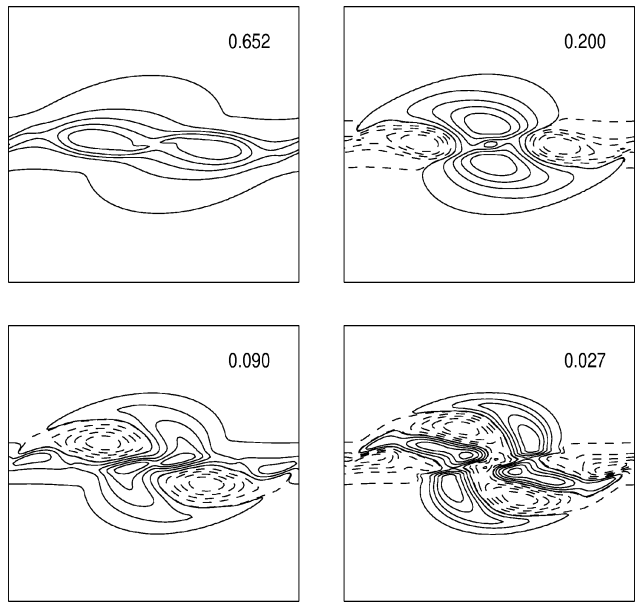

Figure 16. The first four POD structures obtained in a POD analysis for the time-interval [20, 60]. In the pictures solid lines denotes positive vorticity and dashed lines negative. The numbers in the upper-right corner denote the fraction of the energy captured by the corresponding structure.

we can switch from one manifold to another. Another procedure could be based on the distance between the vortices. If the distance is less than the spatial extent of the vortices, we can switch manifold.

- The presented method can be extended to analyze other types of coherent structures. Many coherent structures, such as monopoles, dipoles and tripols, can be described using few parameters, see Van de Fliert, [23]. These descriptions can be used to design a model manifold.
- Another method based on thresholding is also able to yield most of the statistics reported here. Generally time dependent field isolevels at a certain threshold value are used to identify structures. The properties of these structures can be found by integration over the higher isolevel contained within the isolevel characterizing the boundary of the structure.
- To analyse data for which no sensible manifold can be defined, for instance when the origin of the phenomenon is not known a priori, the approach above cannot be applied. Then often a POD method (proper orthogonal decomposition) is employed [24,25]. This method has also been used for the mixing layer, and we compare briefly the results.

  Suitable linear combinations of the various modes of the POD method will reconstruct the signal; see *figure 16* for the most energy containing modes. Additional calculations learned that the principal POD-mode contains 65% of the total energy; this should be compared with the $\mathcal{PM}$ method for which the approximation in $\mathcal{PM}_{\text{Gauss}}$ and $\mathcal{PM}_{\text{Opti}}$, contains 95% and 97% of the total energy respectively. Hence, for the POD method several modes are required for a good reconstruction of the signal. Individually, the modes of the POD analysis show several patches of positive and negative vorticity, but only a suitable linear combination of these modes can represent the Gaussian-type vortices accurately at each instant.

  We can also compare both methods based on the number of degrees of freedom. For instance, for the merging of two vortices we have N^2 ($N = 1$ or 15) degrees of freedom in ϕ for $\mathcal{PM}_{\text{Gauss}}$ and $\mathcal{PM}_{\text{Opti}}$ respectively. In addition we have $6N_T$ degrees of freedom in the parameters. So, in total we have $N^2 + 6N_T = 15^2 + 6 \times 201 \approx 1400$ degrees of freedom for $\mathcal{PM}_{\text{Opti}}$ (≈ 1200 for $\mathcal{PM}_{\text{Gauss}}$). For one POD mode we have the amplitude as parameter, that corresponds to N_T degrees of freedom. Besides

these degrees of freedom, we also have 128^2 degrees of freedom (the number of spatial grid points) in each POD mode itself. Hence, in total the degrees of freedom is larger in the POD method than in the presented method. The difference is that the POD method is a linear method, while the presented method is nonlinear.

The $\mathcal{PM}$ method not only provides more detailed information with one structure, but also the dynamics of the parameters provides physical interpretable information, such as the trajectories of the vortices, their orientation and the length of the main axes provided the vortices are well separated. These quantities cannot be obtained directly in the POD analysis.

References

[1] Van Geffen J.H.G.M., Meleshko V.V., Van Heijst G.J.F., Motion of a two-dimensional monopolar vortex in a bounded rectangular domain, Phys. Fluids 8 (9) (1996) 2393–2399.
[2] Melander M.V., Zabusky N.J., Stycczek A.S., A moment model for vortex interactions of the two-dimensional Euler equations. Part 1. Computational validation of a Hamiltonian elliptical representation, J. Fluid Mech. 167 (1986) 95–115.
[3] Ting L., Klein R., Viscous Vortical Flows, Lecture Notes in Physics, Springer-Verlag, Berlin, 1990.
[4] Corcos G.M., Lin S.J., The mixing layer: deterministic models of a turbulent flow. Part 2. The origin of the three-dimensional motion, J. Fluid Mech. 139 (1984) 67–95.
[5] Corcos G.M., Sherman F.S., The mixing layer: deterministic models of a turbulent flow. Part 1. Introduction and the two-dimensional flow, J. Fluid Mech. 139 (1984) 29–65.
[6] Ho C.M., Huerre P., Perturbed free shear layers, Annu. Rev. Fluid Mech. 16 (1984) 365–425.
[7] Lesieur M., Staquet C., Le Roy P., Comte P., The mixing layer and its coherence examined from the point of view of two-dimensional turbulence, J. Fluid Mech. 192 (1988) 511–534.
[8] Moser R.D., Rogers M.M., The three-dimensional evolution of a plane mixing layer: pairing and transition to turbulence, J. Fluid Mech. 247 (1993) 275–320.
[9] Rogers M.M., Moser R.D., The three-dimensional evolution of a plane mixing layer: the Kelvin–Helmholtz rollup, J. Fluid Mech. 243 (1992) 183–226.
[10] Sandham N.D., Reynolds W.C., A numerical investigation of the compressible mixing layer, Report No. TF-45, Thermosciences Division, Department of Mechanical Engineering, Stanford University, 1989.
[11] Vreman B., Geurts B., Kuerten H., Large-eddy simulation of the turbulent mixing layer, J. Fluid Mech. 339 (1997) 357–390.
[12] Vreman B., Direct and Large-Eddy Simulation of the Compressible Turbulent Mixing Layer, University of Twente, The Netherlands, 1995.
[13] Batchelor G.K., An Introduction to Fluid Dynamics, Cambridge University Press, Cambridge, 1970.
[14] Bernal L.P., Roshko A., Streamwise vortex structure in plane mixing layers, J. Fluid Mech. 170 (1986) 499–525.
[15] Monkewitz P.A., Huerre P., Influence of the velocity ratio on the spatial instability of mixing layers, Phys. Fluids 25 (7) (1982) 1137–1143.
[16] Blumen W., Shear layer instability of an inviscid compressible fluid, J. Fluid Mech. 40 (1970) 769–781.
[17] Michalke A., On the inviscid instability of the hyperbolic-tangent velocity profile, J. Fluid Mech. 19 (1964) 543–556.
[18] Michalke A., Vortex formation in a free boundary layer according to stability theory, J. Fluid Mech. 22 (1965) 371–383.
[19] Ragab S.A., Wu J.L., Linear instabilities in two-dimensional compressible mixing layers, Phys. Fluids A 1 (6) (1989) 957–966.
[20] IJzerman W.L., Signal Representation and Modeling of Spatial Structures in Fluids, University of Twente, The Netherlands, 2000.
[21] Ciarlet P.G., Introduction to Numerical Linear Algebra and Optimization, Cambridge University Press, Cambridge, 1989.
[22] Benzi R., Patarnello S., Santangelo P., Self-similar coherent structures in two-dimensional decaying turbulence, J. Phys. A-Math. Gen. 21 (1988) 1221–1237.
[23] Van de Fliert B.W., Variational Formulations for Coherent Vortex Structures, University of Twente, The Netherlands, 1991.
[24] Berkooz G., Holmes P., Lumley J.L., The proper orthogonal decomposition in the analysis of turbulent flows, Annu. Rev. Fluid Mech. 25 (1993) 539–575.
[25] Holmes P., Lumley J.L., Berkooz G., Turbulence, Coherent Structures, Dynamical Systems and Symmetry, Cambridge University Press, Cambridge, 1996.